FULLY-EMBEDDED PRESSURE SENSOR FOR AERODYNAMICS SURFACES BASED ON FBG TECHNOLOGY

Pietro E. Boffa[2], Emanuele Casciaro[1,3] & Paolo Bettini[1,4]

[1]Department of Aerospace Science and Technology, Politecnico di Milano
[2]pietroedoardo.boffa@mail.polimi.it, +39 339 384 3418
[3]emanuele.casciaro@mail.polimi.it, +39 327 299 8658
[4]paolo.bettini@mail.polimi.it, +39 349 617 7919

Abstract

Static pressure measurements in the aerospace sector are essential for evaluating the performance of aircraft or models in wind tunnels. Currently, these measurements are conducted using bulky and complex systems. To overcome these issues, this paper delves into the development of FBG[1]-based sensor for pressure measurement and its integration into aerodynamic components. The prototype is composed of an optical fiber with an FBG sensor that is deformed by an external structure. This structure transfers the pressure load, acting on its surface, to the fiber in the axial direction. Finite Element Method analyses were employed to understand the behavior of the structure and to balance the sensor dimensions with its sensitivity. An initial non-optimized prototype was developed to validate the functionality of the pressure sensor and identify manufacturing challenges. Moreover, embedding smaller pressure sensors within composite panels provided insights into their integration in complex structures. The final phase of the project includes tests of the pressure sensor under actual operating conditions. This preliminary research validates the effectiveness of FBG pressure sensors in aerodynamic components and lays a groundwork for the advancement of this technology. In the future, it will be necessary to further improve the performance of the prototype and execute more complex tests.

Keywords: FBG, pressure sensor, aerodynamic components, embedding and composite materials

1. Introduction

Pressure measurements are crucial for aerodynamic studies in various fields, including automotive, civil, and aerospace sectors. In the aeronautical field, they are essential for obtaining pressure distributions around wing surfaces. These distributions are responsible for aerodynamic forces and, consequently, the performance of aircraft.

Static pressure is a fundamental parameter essential for determining speed, altitude, lift and drag. It is measured using static ports, namely, integrated orifices on the fuselage of the aircraft positioned to capture airflow with minimal disturbances. Alternatively, a Pitot-static tube combines the static ports with a Pitot probe, device used to measure fluid flow velocity[1].

Wind tunnel tests use static pressure data to validate theoretical and computational models. Measurements are taken at various points near the surface of the component, providing spatial pressure distribution and revealing regions of high and low pressure. This information is crucial for optimizing the shape and structural configuration of the component[2].

Pressure data from these points are transmitted to an transducer outside the wind tunnel model using slender tubes. The transducer quantifies the pressure differential using an electronic strain gauge providing accurate and reliable data for aerodynamic analyses [2]. The fundamental issue with this measurement system, in addition to the potential flow disruption, is the complexity and

[1]Fiber Bragg Grating.

bulkiness. This complexity results in a substantial number of capillary tubes to manage within the testing environment.

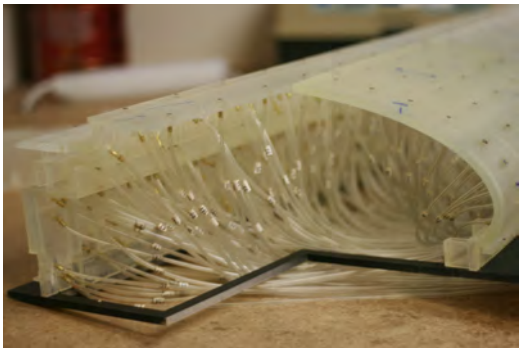

Figure 1 – Leading edge with capillary tubes for measuring static pressure.

Most current pressure sensors rely on capacitive, piezoelectric and piezoresistive mechanisms, which are susceptible to electromagnetic interference. Multipoint pressure measurements with these sensors require the study of the sensor placement on the model surface (array-based design of the measurement system). It adds complexity to the model production and significantly raises the number of measurement wires.[3]
FBG pressure sensors have the potential to replace conventional sensors. They are immune to electromagnetic interference, have compact dimensions, and enable distributed measurements. Multiplexing techniques enable numerous measurement points to be obtained using a single optical fiber. This would significantly reduce the bulkiness of the measurement system. Furthermore, they are well-suited for embedding within composite components. [5][9][10]
Since optical fibers are sensitive to axial deformations, it is necessary to adopt mechanisms that correlate the measured quantity (pressure) to axial deformations of the fibers and increase the sensitivity of the fiber. Some examples include the use of external devices or mechanical structures, as done with metals or polymers.
Metal-based structures include diaphragms, Bourdon tubes, and bellows. **Diaphragms** (2a) are flexible components that deform under pressure, acting as mechanical pressure amplifiers to enhance sensitivity. **Bourdon Tubes** (2b) are hollow metal tubes that elastically deform under pressure, with the FBG sensor within the tube reacting to the deformations. **Bellows** (2c) are elastic components that, under pressure, deform longitudinally an element in which the fibre has been embedded parallel to the direction of strain[4].

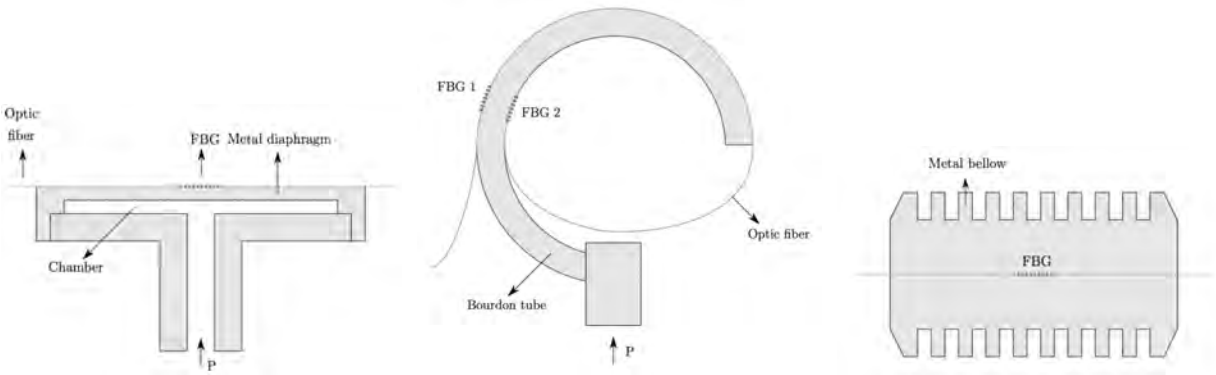

(a) Metal diaphragms-based sensor.

(b) Bourdon tube-based sensor.

(c) Metal bellows-based sensor.

Figure 2 – FBG fibre optic sensors for static pressure measurements using metal-based structures. Figures taken from [11], with permission.

Polymer-based structures include polymer diaphragms and materials for coating the fibers or filling

them. **Polymer Diaphragms** (3a) have a low Young's modulus, its easy deformability enables the FBG sensor to be highly sensitive to pressure changes. One example can be a POFBG[2] bonded to a thin vinyl diaphragm that works similarly to metal diaphragms but with a low Young's modulus. **Polymer Coating/Filling** (3a) consists of coating or embedding the FBG in a polymer medium with a low Young's modulus. The strain applied to the fibre is determined by the polymer, increasing pressure sensitivity. To counteract radial pressure, the FBG can be enclosed in a thick-walled aluminium cylinder. **Axial Strain Amplification** (3a) consists of enclosing the FBG in an aluminium cylinder partially filled with silicone rubber. In this way axial deformation can be further amplified, improving pressure sensitivity. Holes in the aluminium cylinder prevent radial deformations to affect the sensor[4].

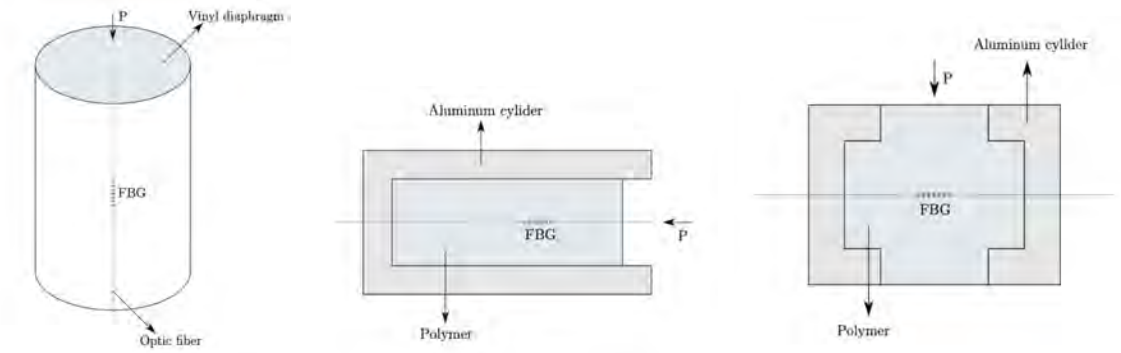

(a) Polymer Diaphragms-based sensor.

(b) Polymer Coating/Filling-based sensor.

(c) Axial Strain Amplification sensor.

Figure 3 – FBG sensors for static pressure measurements using polymer-based structures. Figures taken from [11], with permission.

By leveraging these mechanical structures, FBG pressure sensors can achieve higher sensitivity and reliability, making them suitable for various applications.
The disadvantage of these FBG-based pressure sensors is their inability to be fully embedded within a composite component. This is because they are based on structures with FBG sensors bonded to their surface and have geometries that are incompatible with full embedding.
This work aims to develop a pressure sensor based on FBG technology that can be embedded within aerodynamic composite components, leaving a seamless surface free of any flow disruption. The strategy outlined in this study involves the use of FBG sensor with a mechanism designed to convert the pressure acting on aerodynamic surfaces into axial deformation of the fibre. The final prototype also enables a second strain-free FBGS[3] to be inserted into the pressure sensor for temperature detection. It enhances the versatility of the measurement system.
This article is structured as follows. Section 2. outlines the sensor development process, which includes FEM analyses, conducted to validate the concepts (2.1), and presents the designs derived from various iterations (2.2, 2.3 and 2.4). It also includes a descriptive part of manufacturing tests performed to assess feasibility and sensor impermeability (2.5). Finally, it describes the experimental tests conducted on the final prototype (2.6). Section 3. shows the results of the analysis of each version of the pressure sensor. The outcomes of sensor feasibility tests (3.5) and tests applying pressure with weights (3.4) are described. In the last section, the results obtained from tests with the instrument used to check the pressure applied to the sensor are highlighted (3.6). Section 4. reports the discussion while section 5. presents conclusions and future developments.

2. Methodologies

The sensor was developed from scratch, following an iterative process to achieve a pseudo-optimal and functional prototype. FEM models were employed to evaluate conceptual ideas, determine appropriate dimensions and select suitable materials. Experimental tests were conducted to assess the

[2] Polymer Optical Fiber Bragg Grating.
[3] Fiber Bragg Grating Sensor.

functionality and performance of the sensor. This comprehensive approach, combining simulations and empirical validations, ensured the reliability and effectiveness of the final product.

2.1 FEM Analysys

Various pressure sensors were modeled using *Autodesk Inventor* and exported to *Abaqus* for simulations. Three distinct designs were obtained, labeled as *Version 1* (2.1.1), *Version 2* (2.1.2), and *Version 3* (2.1.3). Each version features a substantial design change to reduce size while maximizing FBG deformation. Table 1 summarizes the strategies and data used in the analyses.

Table 1 – Modelling of sensor components for FEM analyses for each component version. Elements used, constitutive laws and materials are shown.

Component	Version	Elements	Constitutive Law	Material
FBGs	1, 2 and 3	Beam	Linear Elastic Isotropic	Glass
Panel	1	Solid	Linear Elastic Anisotropic	GFRP[4]
Elastomer	1	Solid	Hyperelastic	Silicon
Composite Ring	1	Solid	Linear Elastic Isotropic	Epoxy Resin
Composite Spring	2 and 3	Shell	Linear Elastic Lamina	CFRP[5] and GFRP
Preload Spring	3	Shell	Linear Elastic Lamina	GFRP
Upper Skin	2 and 3	Shell	Linear Elastic Lamina	GFRP
Capsule and Plate	1, 2 and 3	Solid	Linear Elastic Isotropic	Aluminium

The aerodynamic load was analyzed using the following formula and data, obtained using XFOIL [5]:

$$\hat{p} = p - p_\infty = \frac{1}{2}\rho_\infty v^2 C_p. \tag{1}$$

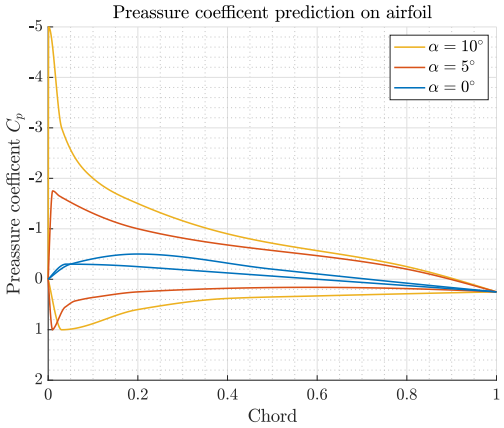

Figure 4 – Comparison of pressure distribution predicted using XFOIL for varying angle of attack.

The analyses were conducted with a coefficient of pressure $C_p = 0.5$. Thus, by modelling the sensor under low pressure conditions, it is possible to ensure that these pressures can be detected and measured effectively. A wind tunnel velocity of $v = 50m/s$ was selected with a standard reference density of $\rho_\infty = 1.225kg/m^3$).

FEM analyses have been followed by representative experimental tests to verify the functionality of the sensors. Moulds were produced for the lay-up of composite components, exploring different geometries. This has allowed for the assessment of all potential risks related to the production and operation of the component.

[4]Glass Fiber Reinforced Polymer.

[5]Carbon Fiber Reinforced Polymer.

2.2 Version 1 Prototype

The *Version 1* of the pressure sensor involves embedding the optical fiber within an elastomeric material. As the elastomer deforms due to pressure, it in turn deforms the fibre, enabling a correlation between pressure and axial deformation of the fibre.
Three different configurations were studied. The first is reported in Figure 5a. The elastomeric block has a simple design, with the pressure sensor partially embedded in the composite structure. The second one, in Figure 5b, was considered to ensure that complete embedding do not compromise sensitivity, while achieving a smooth panel surface. The third configuration was studied to enhance the sensitivity of the component. The shape of the elastomeric tile was modified as shown in Figure 5c, adding a diaphragm to increase its deformation.

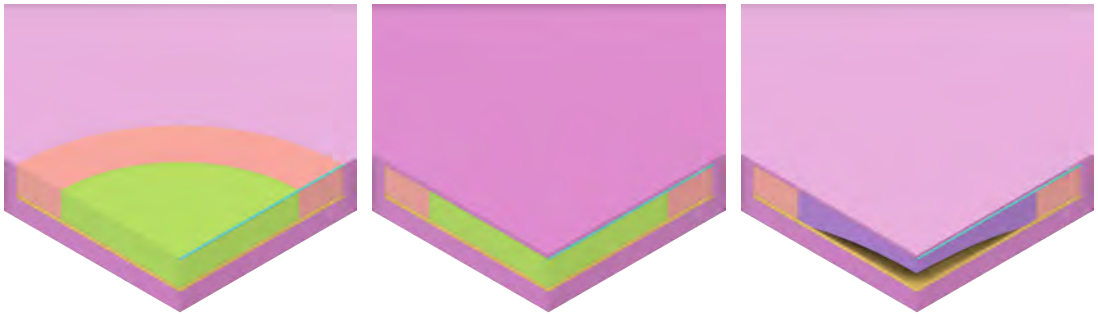

(a) Component partial embedded. (b) Component fully embedded. (c) Component fully embedded with diaphragm.
■ Composite material, ■ Metal plate, ■ Supporting ring, ■ Elastomeric tile (normal), ■ Elastomeric tile (diaphragm) and ■ Optic fiber.

Figure 5 – Prototypes based on an elastomeric tile (1/4 view). Figures taken from [11], with permission.

The results of the sensor sensitivity analysis are reported in the results chapter 3.1 These prototypes were not produced, we proceeded to the design of Version 2 after the FEM analysis.

2.3 Version 2 Prototype

It was decided to add an external mechanism for transferring the load (pressure) from its top surface to the fiber axial direction. Throughout the article, this structure will be referred to as the "composite spring".
Three layers of a thin glass fiber pre-preg, 0.05 mm, was used for the composite spring base. For reinforcement, four layers of 0.28 mm unidirectional glass-fibers were positioned at [0° 90° 90° 0°] angles to create a symmetric laminate, reducing potential warping. Figure 7a shows the lay-up sequence, and Figure 7b illustrates the reinforcement placement. Both the composite spring and reinforcement were cured in a vacuum bag and autoclave at 125℃ under 3 bars of pressure for 1 hour.

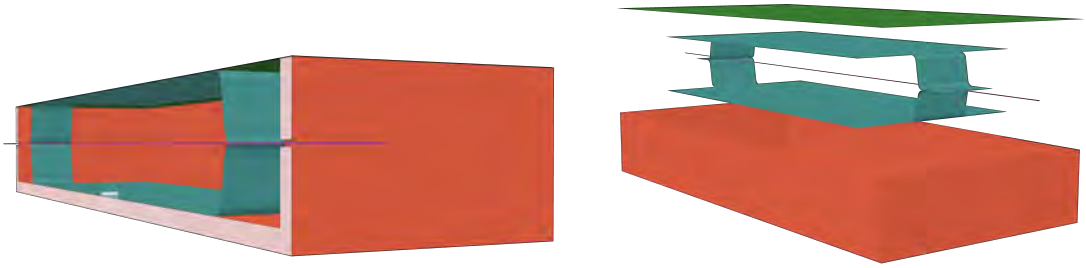

(a) Cross-section of the sensor. (b) Assembly of the sensor.
■ Capsule, ■ Composite spring, ■ Optic fiber and ■ Composite upper skin.

Figure 6 – *Version 2*: pressure sensor based on external structure (composite spring). Figures taken from [11], with permission.

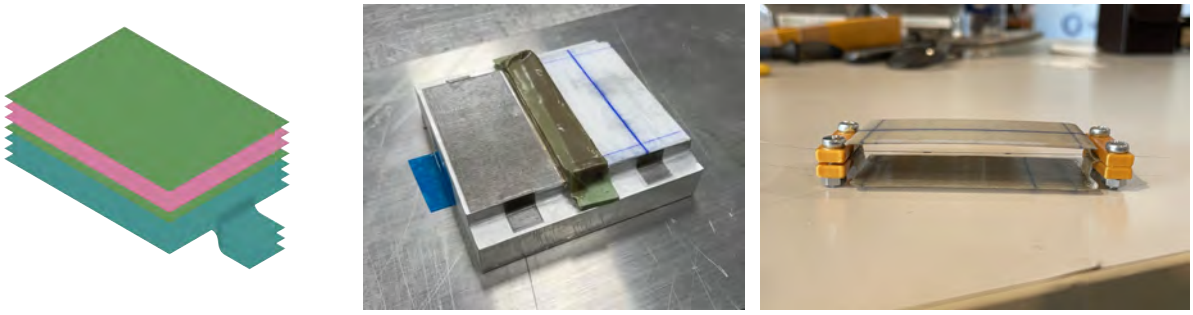

(a) Representation of the lay-up of *Version 2* prototype. (b) Production of *Version 2* prototype. (c) *Version 2* prototype with FBG sensor fixed.
■ Glass fiber fabric 0.05 mm ■ UD glass fiber 0.28 mm 0° and ■ UD glass fiber 0.28 mm 90°.

Figure 7 – Lamination sequence, mold lamination, and testing set-up of *Version 2* prototype. Figures taken from [11], with permission.

To evaluate the sensor functionality, custom 3D-printed PETG[6] clamps were designed to secure the FBG sensor to the composite spring. These clamps were positioned at the hinges of the composite spring and fastened with screw nuts. Figure 7c illustrates the setup with the fiber held by the clamps. Several tests were conducted by placing weights ranging from 5 g to 200 g on the structure to simulate pressure. This enabled the evaluation of the performance of the sensor.

2.4 Version 3 Prototype

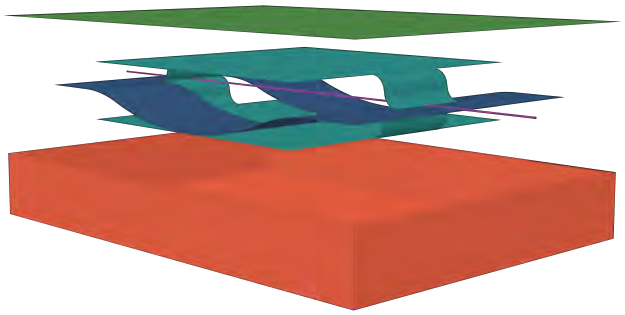

■ Aluminium capsule, ■ Composite spring, ■ Optic fiber, ■ Composite upper skin and ■ Preload composite spring.

Figure 8 – *Version 3*: sensor based on composite spring with preload spring. Figure taken from [11], with permission.

[6]Polyethylene terephthalate glycol is a thermoplastic polyester.

This latest model has been designed to reduce the dimensions of *Version 2*. Due to the small size of this prototype, two elements had to be added to maintain the sensitivity of the sensor: the preload spring and spacer that preload it. The functionality of these two items will be highlighted in (3.3). To enhance precision during the cutting phase of the pre-preg fabric, templates were used (9b). Figure 9a shows the lay-up process of the composite spring, with carbon fiber fabric directly incorporated alongside fiberglass fabric.
In this production batch, the preload spring made of GFRP is also included, with its lay-up shown in Figure 9c. The mold for the preload composite spring is depicted in Figure 9d.

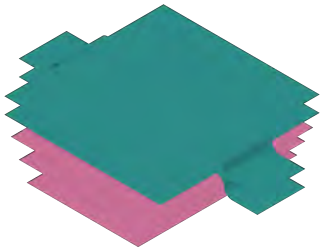

(a) Representation of lay-up of *Version 3* prototype composite spring.

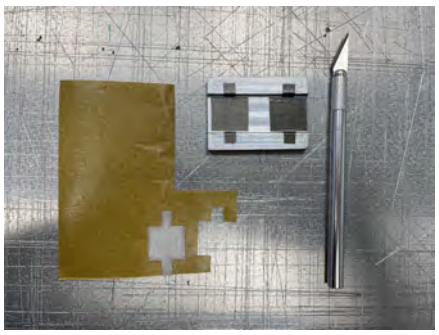

(b) Production of *Version 3* prototype composite spring.

■ Glass fiber fabric 0.05 mm 0° and ■ Carbon fiber fabric 0.10 mm.

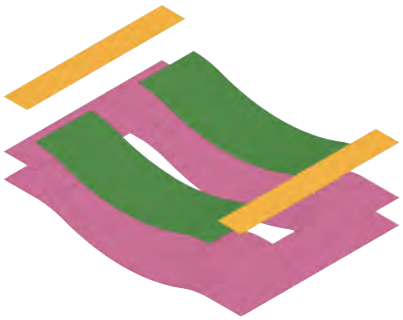

(c) Representation of lay-up of *Version 3* prototype preolad composite spring.

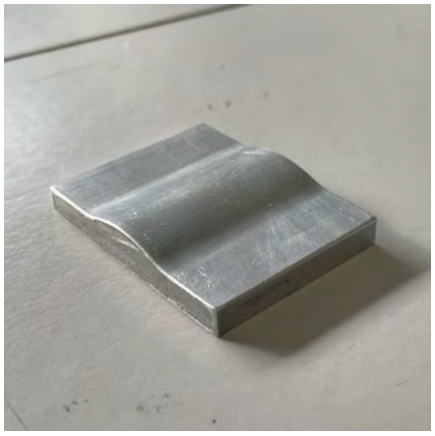

(d) Mold of preload composite spring.

■ UD glass fiber 0.28 mm 90°, ■ Glass fiber fabric 0.05 mm and ■ Glass fiber fabric 0.05 mm.

Figure 9 – Production elements of *Version 3* include laminating sequences for the manufactured components, work tools and the preload spring mold. Figures taken from [11], with permission.

The assembly phase of the various sensor components encompasses several steps and is divided into three stages:

- **Bonding Phase 1 (Figure 10a and 10b)** Attaching the preload spring to the underside of the composite spring using a thermosetting epoxy resin film. Aluminum clamps with silicone tiles ensure uniform pressure without risking component breakage.
- **Bonding Phase 2 (Figure 10c and 10d)** Affixing FBG sensor to the previous assembly, along with the top portion of the composite spring. Tensioning the optical fiber is crucial for accurate measurements. It is achieved by securing the fiber with adhesive tape before bonding.
- **Bonding Phase 3 (Figure 10e, 10f and 10g)** Inserting and bonding of the component realised

to the capsule and bonding the outer skin of the pressure sensor capsule to the structure using epoxy resin patches.

All these steps are performed in an oven at 125℃ for 1 hour.

(a) Representation of bonding phase 1.

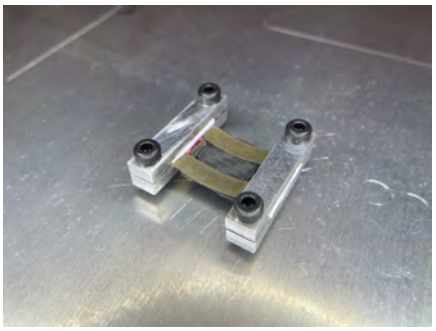

(b) Phase 1 bonding procedure.

■ Composite preload spring, ■ Composite lower spring and ■ Epoxy resin.

(c) Representation of bonding phase 2.

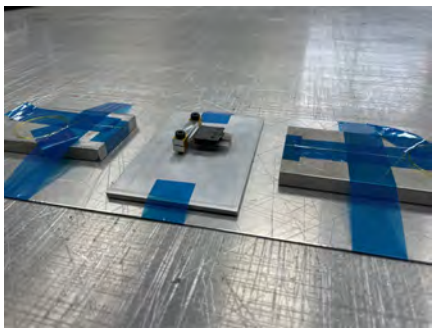

(d) Phase 2 bonding procedure.

■ Composite upper spring, ■ Epoxy resin, ■ Optic fiber and ■ Previous bonding phase.

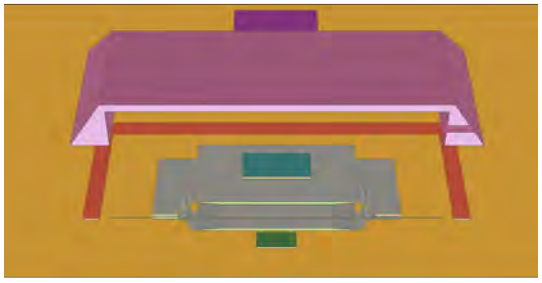

(e) Representation of bonding phase 3.

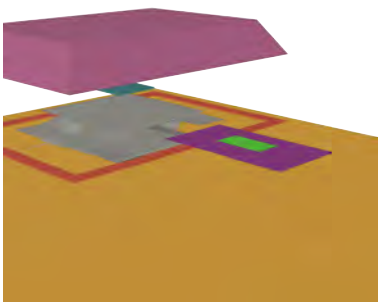

(f) Representation of bonding phase 3 (side view).

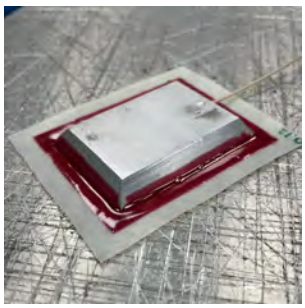

(g) Sensor side view.

■ Epoxy resin seal, ■ Lower epoxy resin patch, ■ Upper epoxy resin patch, ■ Aluminium capsule, ■ Pre-load, ■Pre-load epoxy resin patch, ■ Composite outside skin and ■ Previous bonding phase.

Figure 10 – Sequence of steps required for assembling the various components of the final pressure sensor. Each phase involves oven treatment. Figures taken from [11], with permission.

Version 3 was embedded in a panel made of multiple layers of carbon fiber fabric. The lamination process of the panel is illustrated in Figure 11. In Figure 11a, a distinct pre-preg material is observed near the PEEK[7] tube emerging from the capsule. This material comprises unidirectional carbon fabric pre-preg, facilitating better accommodation of the PEEK tube within the panel.

[7] Polyether ether ketone is a thermoplastic polymer.

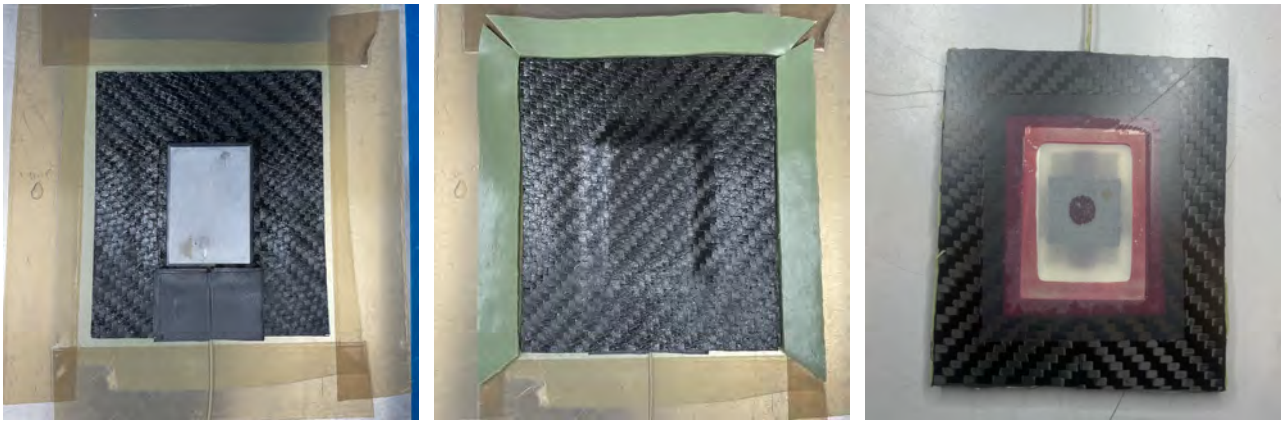

(a) Intermediate phase of lamination. (b) Final phase of lamination. (c) Final phase of lamination.

Figure 11 – Incorporation of final version (*Version 3*) of the prototype into carbon composite panel during lamination phase. Figures taken from [11], with permission.

The panel was polymerized in autoclave for 1 hour at 3 bar and 125℃. The embedding phase was successful and no damage was detected in the pressure sensor.

2.5 Permeability test

Permeability test, simulating the embedding process, were conducted to create a resin-resistant sensor. The embedding phase was simulated by placing these capsules inside a composite panel, replicating the same embedding process as performed on the latest sensor. Various techniques were employed to ensure the impermeability of the sensor. These techniques include the use of a single layer of epoxy resin (Capsule 1), the use of two layers of epoxy resin (Capsule 2), the use of one layer of epoxy resin and one of Kapton (Capsule 3), and the use of a double layer of epoxy resin and the sealing of the internal environment of the capsule (Capsule 4). This latter case enabled the evaluation of the effect of not applying a vacuum inside the capsule during the autoclave curing process. The outcomes of this test are reported in section 3.5

2.6 Preassure Testing and Characterisation

Both *Version 2* and *Version 3* were tested with weights to simulate pressure. The last part of the work focuses on testing prototypes by applying air pressure to the sensor. This approach characterizes the response of the sensor to pressure. *Mensor's CPC6000 modular precision pressure controller* was used to generate precise and uniform pressures. This tool provided specific pressures, which have been applied to the sensor using a hermetic chamber (Figure 12). The deformation of the optical fiber under pressure was measured using a *Micron Optics optical sensing interrogator*.

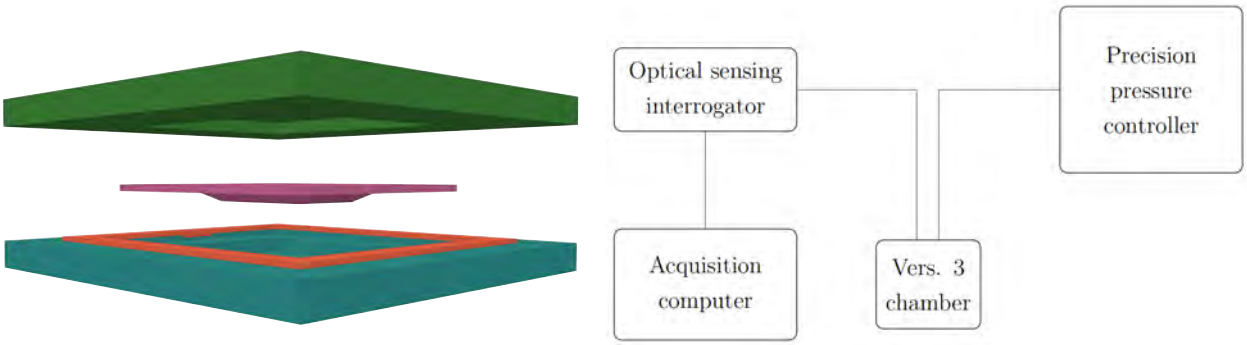

(a) Test chamber side view. (b) Experiment setup diagram.

■ Lower half of chamber, ■ Upper half of chamber, ■ Panel with sensor and ■ Silicon seal.

Figure 12 – Sealed chamber for pressure maintenance and schematic diagram of experimental system used in tests at various pressure levels. Figures taken from [11], with permission.

Figure 12b provides a schematic of the connections of the various instruments. The *"Version 3 chamber"* was connected to the precision pressure controller and the optical fiber was connected to the Optical Sensing Interrogator. The precision pressure controller software enables setting a pressure range from -20000 Pa to 20000 Pa. Meanwhile, the acquisition computer displays the wavelength variation due to applied pressure.
For sensor characterization, two tests were conducted: one with positive pressure, where the pressure vector is opposite to the vector normal to the sensor surface, and one with negative pressure, where the pressure vector is aligned with the vector normal to the sensor surface. The pressure controller set the desired pressure, and after a brief period to achieve equilibrium, wavelength readings from the FBG sensor were acquired. Continuous pressure modulation was not available; adjustments have been made in discrete steps with transient periods for stabilization. A *MATLAB* function was developed to analyze the data by interpreting the wavelength reflected by the FBG sensor. This function identifies step transitions by evaluating deviations from the average of preceding points, selecting a point just before the transition where pressure equilibrium is achieved.
In addition to the sensor characterization tests, other tests was conducted to assess the accuracy and repeatability of the sensor by performing the same measurements several times.

3. Results

3.1 FEM Analysis: Version 1

The fiber optic displacements of the three configurations, described in Figure 5, are shown in the bar chart below. The deformations, considering the load presented in the chapter 2.1, are low for all the cases studied.

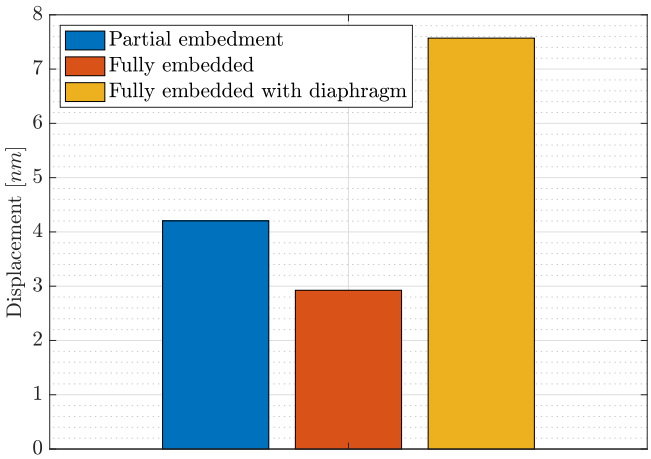

Figure 13 – Bar chart comparing deformations of optical fiber in configurations of *Version 1* previously reported with load described in 2.1 Figure taken from [11], with permission.

The results show that the axial displacement of a fiber embedded in an elastomeric tile is limited. This is due to the low pressure, to the material considered and to the limited deformation of the elastomer in the plane on which the fiber lies. Furthermore, the axial strain of the fiber is a secondary effect of pressure action due to the volumetric deformation of the elastomer.
As shown in Figure 13, the displacement in the partial embedded component and fully embedded component are quite similar. It is therefore possible to conclude that the total encapsulation of the sensor results in a limited loss of sensitivity. This offers the possibility of obtaining a smooth outer surface that does not disturb the aerodynamic flow.

3.2 FEM Analysis: Version 2

Compared to *Version 1*, it was decided not to use elastomeric materials and to add the external mechanism, described previously, to enhance the axial deformation of the fiber under the effect of pressure.

During the design phase of *Version 2*, analytical and numerical analyses were conducted with the aim of maximizing the deformation of the fiber due to the load acting on the structure. These studies are reported below.

Dimension of the composite spring

A two-dimensional approximated system helped to identify geometric parameters that enhance deformation transfer. Half of the composite spring was modeled with rigid beam elements. The fixed parameters included Young's modulus and the cross-sectional area of the optical fiber. The structure was constrained to the ground with two hinges, one fixed and the other able to move horizontally.
The analysis applied uniform pressure p to the upper part of the spring over the area ab, yielding force $F = pab$. The reaction force R on the optical fiber depended on the pressure application surface (a) and (b), spring height (h), and angle (θ).

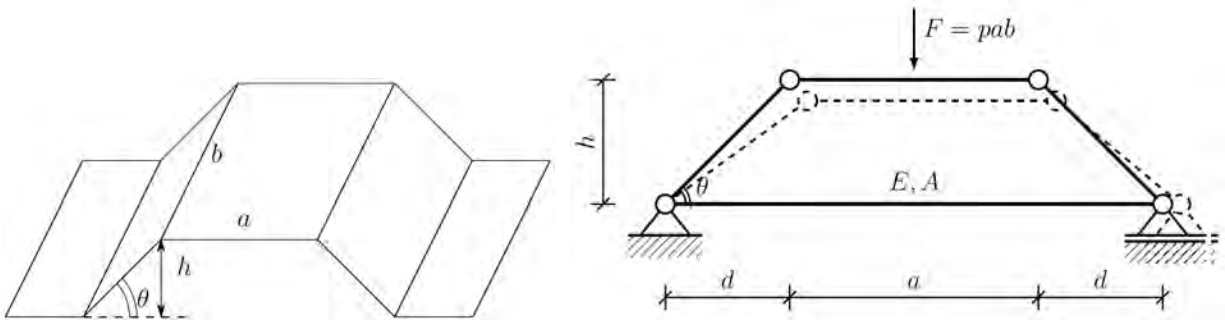

(a) Cross-section of the pressure sensor. (b) Assembly of the pressure sensor.

Figure 14 – Representative 2D diagram of composite structure and optical fibre. Figures taken from [11], with permission.

The momentum equilibrium equation at the left upper hinge was considered to evaluate the parameters that significantly influenced the deformation of the optical fiber. The fiber was modeled as spring with stiffness $k = EA/(2h\tan\theta + a)$. Infinitesimal deformations resulted in spring deformation $\Delta l = R/k$.

$$\Delta l = \frac{pab}{2}\tan\theta\frac{2h\tan\theta + a}{EA} \rightarrow \Delta l = \frac{p}{2EA}(2abh\tan^2\theta + a^2 b\tan\theta). \tag{2}$$

The elongation of the fiber is mainly influenced by the angle (θ) and the length (a), because of the terms $\tan^2\theta$ and a^2. An 80° angle was chosen for prototypes to balance sensitivity, stability and manufacturing feasibility.

Composite spring reinforcement

Another aspect that reduces the sensitivity of the pressure sensor is the rigidity of the upper section. Initial sensor analyses revealed that pressure on the top structure surface causes deformation in the upper part of the composite spring, reducing deformation transfer to the fiber.
This phenomenon is illustrated in Figure 15. To address this issue, reinforcing the upper section of the composite spring was necessary. FEM simulations enabled the evaluation of the addition of composite materials on the upper surface of the structure to reinforce it. Figure 15 shows two examples: the model with three carbon fiber fabric plies (15a) and the model with eight carbon fiber fabric plies (15b). The contribution of the reinforcement to the deformation of the upper surface is highlighted. During manufacturing, the available material, which was 4 layers of unidirectional glass-fibers, was used.

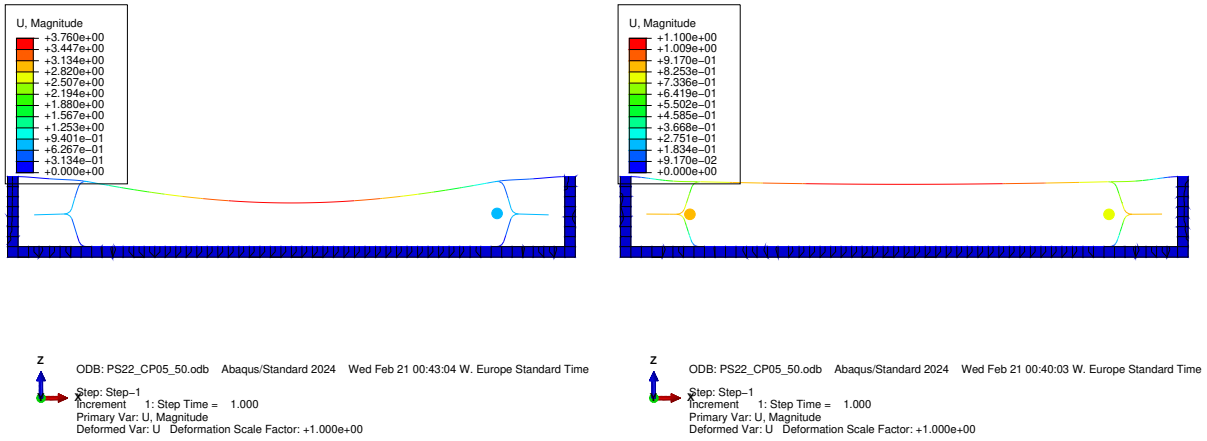

(a) Poor reinforcement.

(b) Optimal reinforcement.

Figure 15 – Effect of reinforcement on upper composite spring. Figures taken from [11], with permission.

Composite spring side walls

The side walls of the composite spring stiffened the structure at the connection points, reducing the deformation transferred to the fiber. It was therefore necessary to reduce the stiffness of these parts of the structure. Figure 16 highlights the material removal to improve composite spring flexibility at the hinges.

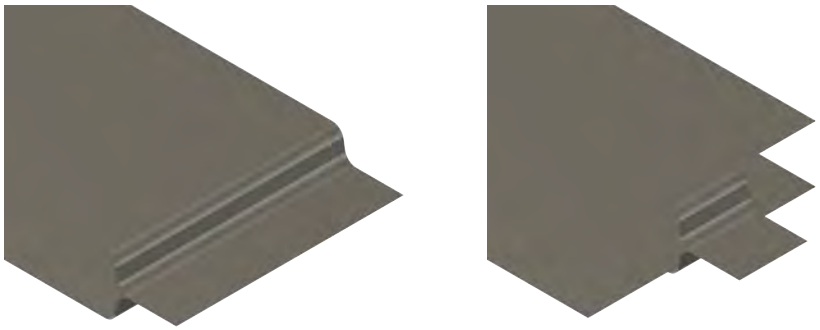

(a) Normal composite spring.

(b) Weakened composite spring.

Figure 16 – Weakening of side walls of composite spring to increase its compliance in order to transfer more strain to optical fibre. Figures taken from [11], with permission.

Interaction with composite spring, composite upper skinand capsule

Another aspect considered was the gap between the composite spring and the capsule walls enclosing the optical fiber. The composite spring is connected to the capsule by the outer skin, which is subjected to aerodynamic flow. The deformation of the composite spring induces a force on the outer skin that is constrained by the metal capsule. This reduces the displacement of the structure due to pressure.

An optimal value exists for this gap. Enlarging the gap decreases the force that restricts composite spring deformation. Excessive increments can cause over-deformation of the outer skin, preventing effective transfer of its deformation to the composite spring top surface. Determining this optimal distance involved adjusting the capsule size, increasing it until excessive outer skin deformation occurred. The optimal distance was found to be 4 mm.

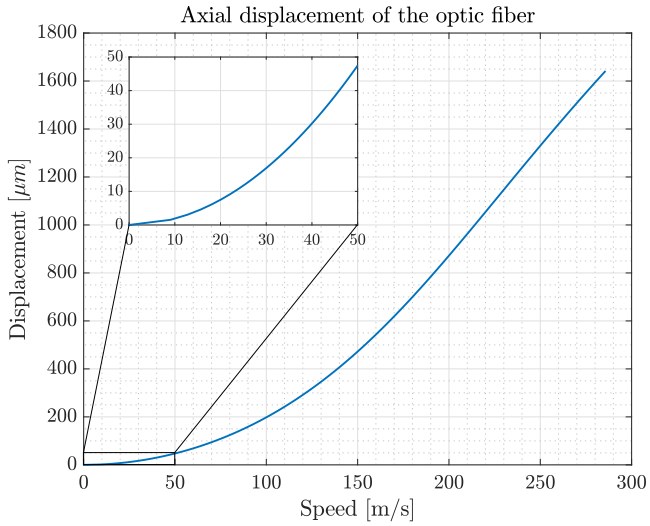

Figure 17 – Deformation of optic fiber with speed, responsible for pressure on aerodynamic surfaces. Figure taken from [11], with permission.

From Figure 17, it can be seen that *Version 2* shows significant improvements compared to *Version 1*, with considerable fiber displacement and high stress transfer capability. The drawback of *Version 2* was its size, measuring 81 mm x 39 mm x 11.5 mm. However, the larger dimensions of this component have favored its production as a Proof of Concept to verify the operational mechanism of the sensor before proceeding with the development of the *Version 3* prototype.

3.3 FEM Analysis: Version 3

In this section, various strategies have been introduced to reduce the size of the pressure sensor, from *Version 2* to *Version 3*, while maintaining its sensitivity.
Reducing sensor dimensions decreases sensitivity due to the reduced surface area exposed to pressure. To mitigate this issue, an external mechanism has been proposed to enhance sensitivity at low speeds by inducing deformation. This mechanism, functioning as a preload spring, maximizes its effect at low speeds and gradually diminishes its influence as aerodynamic load increases.
The preload spring, made of thin GFRP laminate, is bonded in the same area as the optical fibre, as shown in Figure 8. A spacer, between the preload springs and the composite spring, regulates the preload. Thicker spacers result in higher preload.

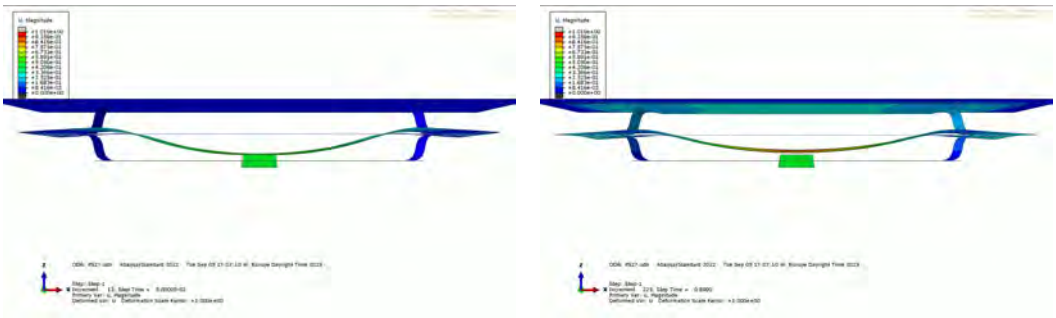

(a) High contribute. (b) Null contribute.

Figure 18 – Preload spring contribution under two different sensor operating conditions. Low flow velocities (a) and high flow velocities (b). Figures taken from [11], with permission.

At low speeds (Figure 18a), the preload mechanism enhances sensor operation. Its contribution gradually decreases with increasing pressure. Once disengaged from the preload spacer, the preload spring ends its contribution (Figure 18b).
The preload spring offers self-protection at high velocities, resisting excessive sensor deformation. Additionally, it enables the optical fiber to work under compression, ensuring operational continuity

even under opposite external pressure.

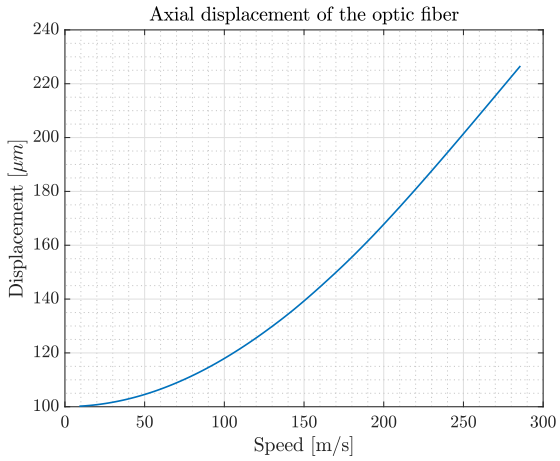

Figure 19 – Axial displacement of optic fiber with speed, responsible for pressure on aerodynamic surfaces. Figure taken from [11], with permission.

In Figure 19, it is possible to appreciate the performance of the component in terms of the axial displacement imposed on the optical fibre, particularly at low velocities. Compared to *Version 2,* the sensor measures 35mm x 25mm x 4.5mm, representing an 89 % reduction in volume.

3.4 Weights tests

These tests involved placing weights on the composite spring upper surface at least five times to ensure consistency and repeatability. These tests are conducted to verify the correct operation of the sensor and ensure the functionality of its mechanism. The data collected was filtered using a fourth-order Butterworth filter and processed with a MATLAB algorithm to identify load and unload states, computing the corresponding $\Delta\lambda$ values. Here are reported the results of the weight tests.

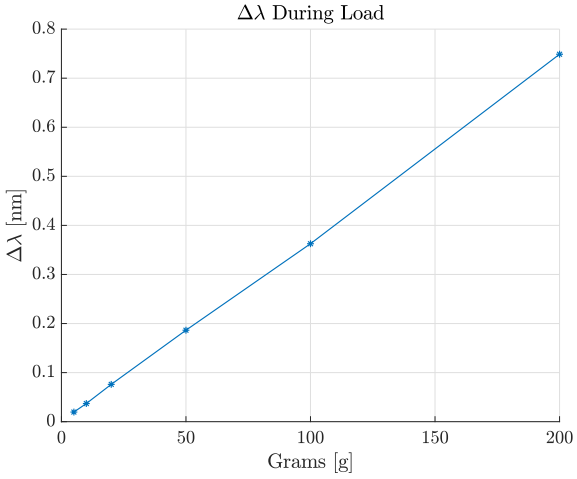

Figure 20 – Variation of Bragg wavelength reflected by the sensor while adding representative pressure weights to the surface of *Version 2* composite spring. Figure taken from [11], with permission.

Figure 20 demonstrates the sensor performance, exhibiting sensitivity even to low weights. The same tests were conducted on *Version 3* to evaluate the sensor sensitivity after size reduction. Preload spacers of different dimensions were considered to evaluate their effectiveness.
The results, shown in Figure 21, indicate accurate measurement of low weights. Preloading enhances performance by approximately 30%, although a specific trend in improvement with varying preload

spacers is not evident. One possible factor is the slight variations in weight positioning that contribute to this variability.

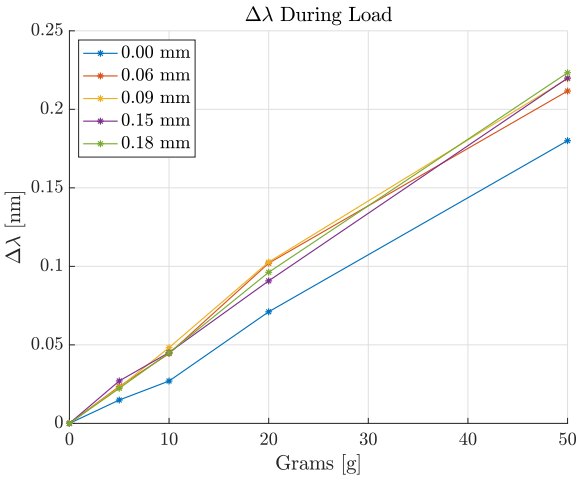

Figure 21 – Variation of Bragg wavelength reflected by the sensor while adding representative pressure weights to the surface of *Version 3* composite spring and varying the preload. Figure taken from [11], with permission.

3.5 Manufacturing tests

For impermeability tests, the embedding process, depicted in Figure 22a, was conducted on a single panel. In Figure 22b, the various capsules can be observed during the embedding process. The vacuum bag from this process was then placed in an autoclave for polymerization at 3 bars and 125℃ for one hour.

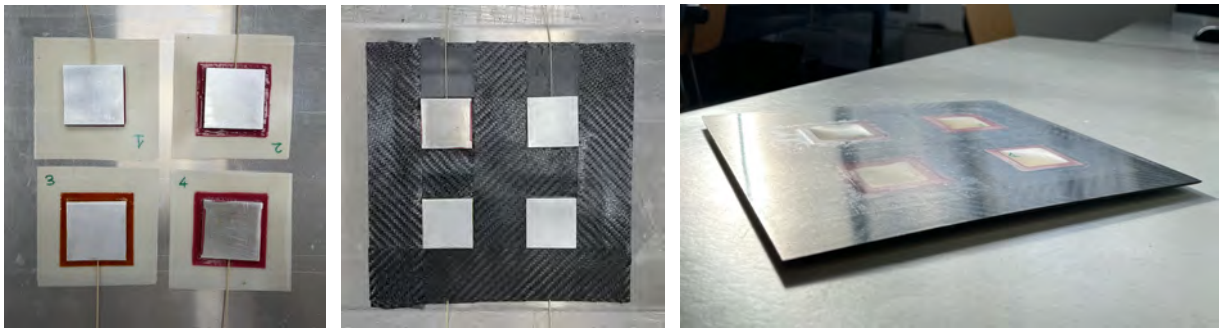

(a) Capsule arraignment. (b) Lamination process. (c) Permeability test side view.

Figure 22 – Permeability testing of the sensor within the structure. Various strategies were employed to prevent the formation of holes and the ingress of resin. Figures taken from [11], with permission.

The test results demonstrate effective prevention of resin ingress into the internal sensor environment for all solutions. Notably, Capsule 4 exhibited unique behavior compared to the other tests. It did not display inward deformation of the outer membranes within the panel (Figure 22c). This difference resulted from the isolation of the internal capsule environment. In Tests 1, 2, and 3, the capsule interior was under vacuum, leading to inward deformation of the outer skin. Capsule 4 experienced internal pressure pushing the outer skin outward.

3.6 Pressure tests

The resulting data makes it possible to draw up a characteristic curve that relates the reflected wavelength to the pressure. As shown in Figure 23a, the sensor measures a wide range of pressures and manages low pressures accurately. Figure 23b reveals that between -5000 Pa and 5000 Pa, the sensor response is nonlinear, likely due to the preload spring influence. Outside this range, the sensor exhibits highly linear characteristics.

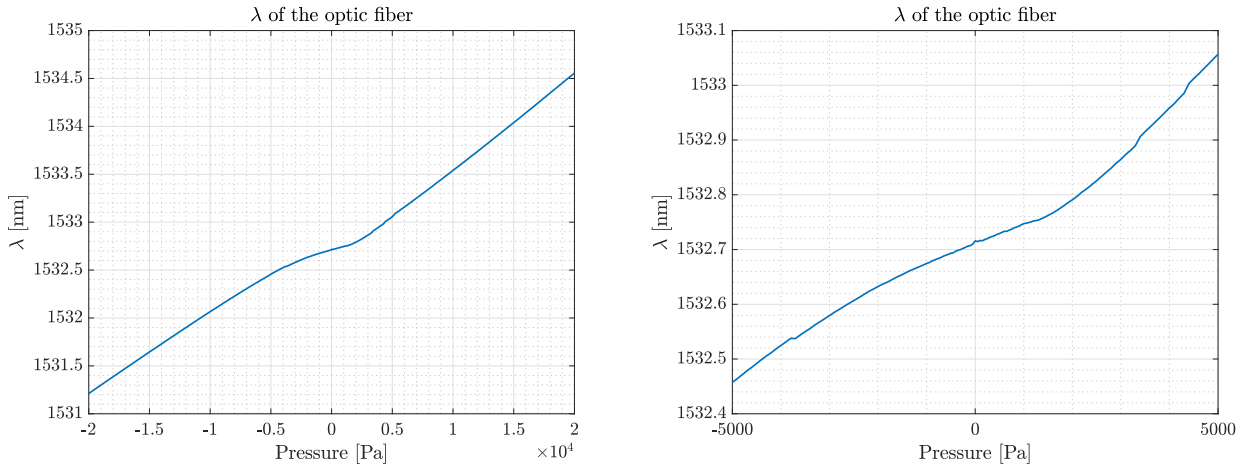

(a) Range -20000 Pa to 20000 Pa.

(b) Range -5000 Pa to 5000 Pa.

Figure 23 – Variation of reflected Bragg wavelength with respect to pressure applied by instrument. Full operating range (a), non-linear part of sensor characteristic curve (b). Figures taken from [11], with permission.

After defining the characteristic curve, cyclic loading and unloading tests were performed. This tests involve cycling between 15000 Pa and -15000 Pa. Figure 24 depicts a slight hysteretic trend. The system response during loading and unloading cycles is very similar, with overlapping curves in Figure 24. This indicates that the error observed in measurements is mainly due to the sensor history from previous loading and unloading conditions. The maximum deviation occurs where the pressure is zero but the sensor measures 22.7 pm.

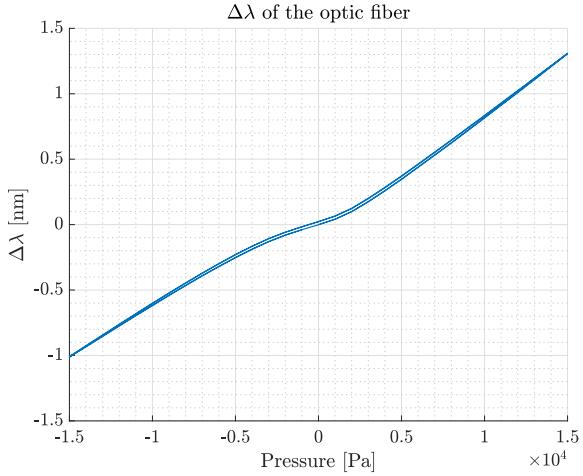

Figure 24 – Cyclic testing of sensor loading and unloading in test instrument for accuracy and repeatability assessment (-15000 Pa – 15000 Pa). Figure taken from [11], with permission.

4. Discussion

The following section discuss the results and analyses from various tests conducted to evaluate the sensor performance. These tests include weight assessments, manufacturing evaluations, and pressure controller analyses, all aimed at ensuring the sensor accuracy under different conditions.
Weight tests were crucial, confirming the functionality of the sensor mechanism and revealing the impact of preloading on Version 3. Preloading improved performance by approximately 30% compared to the unloaded case. Manufacturing tests, aimed at preventing resin ingress into the capsule, resulted in a smooth sensor surface without inward deformation.
Pressure controller tests demonstrated that the sensor could detect pressure variations as low as 50 Pa, suitable for wind tunnel applications. The limits of the pressure range (-20000 Pa to 20000

Pa) are due to the testing instrument. The sensor can potentially measure higher pressures. This indicates a wide operational range due to its high sensitivity at both low and high pressures.
It also guarantees the possibility of making differential pressure measurements, which are more useful in the aviation sector.
Slight hysteresis observed in loading and unloading tests is likely due to the materials used, specifically the thermosetting epoxy resin employed in bonding processes. This viscoelastic properties of this resin cause creep, leading the sensor to maintain a deformed state when loads change, resulting in measurement deviations. Careful material selection would enhance sensor accuracy and sampling frequency. Therefore, the slow response of the sensor to rapid pressure changes is attributed to resin creep and to the influence of air inside the sensor, which moves through the optical fiber inlet pipe.[7][8]

5. Conclusions and Future developments

The FBG sensors exhibited excellent sensitivity and accuracy in detecting pressure changes, underscoring their suitability for static pressure monitoring tasks.
The results with the pressure controller demonstrated that the sensor could detect pressure variations as small as 50 Pa. A slight hysteretic trend is observed, limiting the sampling frequency. The system response during loading and unloading cycles is very similar. This indicates that measurement errors are mainly due to the sensor history from previous loading conditions.
The successful completion of the bonding steps ensured solid encapsulation of the sensor components, resulting in a compact sensor package that is easy to integrate into the lamination phase of a component.
Various strategies are available to address epoxy resin creep, such as incorporating additives (like glass microspheres) or reinforcing fibers to improve dimensional stability, and applying post-curing heat treatments to reduce residual stresses.
The structural isolation of the FBG enables temperature measurements that can enhance sensor accuracy and versatility. Future efforts should focus on increasing production volume, refining processes to reduce labor intensity.
Multiplexing techniques may facilitate integrating multiple sensor packages on a single optical fiber, boosting sensor density and monitoring capabilities.
Further miniaturization of the sensor remains an area for potential development.
This technology has possible applications in various sectors. From advanced military aerospace to commercial aviation and competitive automotive sectors. Civil and transportation industries could also benefit from its flexibility and precision.

6. Copyright Statement

References

[1] E.H.J. Pallett. *Aircraft Instruments and Integrated System*. 1st edition, Prentice Hall. 1992.

[2] J.B. Barlow, Wi.H. Rae, Jr and A. Pope. *Low-Speed Wind Tunnel Testing*. 3rd edition, John Wiley and Sons, Inc. 1999.

[3] C.R. Spitzer, U. Ferrell and T. Ferrel. *Digital Avionics Handbook*. 3rd edition, CRC Press. 2015.

[4] Siyi Xu, Xiaozhi Li, Tanyu Wang, Xiujuan Wang and Hao Liua. Fiber Bragg grating pressure sensors: a review. *Optical Engineering*, Vol. 62, No. 1, 010902, Tiangong University. 2023.

[5] A. G. Simpson *Optical Fibre sensors and Their Interrogation*. Doctoral Thesis, Aston University. 2005.

[6] M. McCarty *The Measurement of the Pressure Distribution over the Wing of an Aircraft in Flight*. Master Thesis, University of New South Wales. 2008.

[7] H.L. Ornaghi Jr, J.H.S. Almeida Jr, F.M. Monticeli, R.M. Neves, M.O.H. Cioffi. Time-temperature behavior of carbon/epoxy laminates under creep loading. *Mech Time-Depend Mater*, Vol. 25, pp. 601–615, Springer. 2021.

[8] F.M. Monticeli, H.L. Ornagh Jr, R.M. Neves and M.O.H. Cioffi. Creep/recovery and stress-relaxation tests applied in a standardized carbon fiber/epoxy composite: Design of experiment approach. *The Journal of Strain Analysis for Engineering Design*, Vol. 55, pp. 109-117. 2020.

[9] Yun-Jiang Rao. In-fibre Bragg grating sensors. *Measurement Science and Technology*, Vol. 8, No. 4, pp. 355-375. 1996.

[10] A.D. Kersey, M.A. Davis, H.J. Patrick, M. LeBlanc, K.P. Koo, C.G. Askins, M.A. Putnam and E.J. Frieb. Fiber Grating Sensors. *Journal of Lightwave Technology*, Vol 15, No. 8, p. 1442. 1997.

[11] P.E Boffa *Fully-Embedded Pressure Sensor For Aerodynamics Surfaces Based on FBG Technology*. Master Thesis. Politecnico di Milano. 2024.